Hydrogen embrittlement and its prevention in 7XXX aluminum alloys with high Zn concentrations

Shimizu, Kazuyuki
Department of Physical Science and Materials Engineering, Iwate University

Toda, Hiroyuki
Department of Mechanical Engineering, Kyushu University

Fujihara, Hiro
Department of Mechanical Engineering, Kyushu University

Yamaguchi , Masatake
Center for Computational Science and e-Systems, Japan Atomic Energy Agency

他

https://hdl.handle.net/2324/7160861

出版情報：CORROSION. 79 (8), pp.818-830, 2023-08-01. Association for Materials Protection and Performance (AMPP)
バージョン：
権利関係：

Hydrogen embrittlement and its prevention in 7XXX aluminum alloys with high Zn concentrations

Kazuyuki Shimizu[‡], Hiroyuki Toda**, Hiro Fujihara**, Masatake Yamaguchi***, Masayuki Uesugi****, Akihisa Takeuchi****, Masahiko Nishijima***** and Yasuhiro Kamada**

[‡]Corresponding author. E-mail: ksmz@iwate-u.ac.jp

* Department of Physical Science and Materials Engineering, Iwate University, 4-3-5 Ueda, Morioka City, Iwate, 020-8551, Japan.

** Department of Mechanical Engineering, Kyusyu University, 744 Motooka, Nishi-ku, Fukuoka City, Fukuoka, 819-0395, Japan

*** Center for Computational Science and e-Systems, Japan Atomic Energy Agency, 2-4 Shirakata, Tokai-mura, Ibaraki, 319-1195, Japan

**** Japan Synchrotron Radiation Research Institute, SPring-8, 1-1-1 Kouto, Sayo-cho, Hyogo, 679-5198, Japan.

***** Flexible 3D System Integration Laboratory, Sanken, Osaka University, 8–1 Mihogaoka, Ibaraki City, Osaka, 567-0047, Japan

ABSTRACT

7xxx aluminum alloys are representative high-strength aluminum alloys; however, mechanical property degradation due to hydrogen hinders further strengthening. We have previously reported that hydrogen embrittlement in 7xxx alloys originates from trapped hydrogen at the $MgZn_2$ precipitate interface, providing high hydrogen trapping energy. We propose the dispersion of Mn-based second-phase particles as a novel technique for preventing 7xxx aluminum alloy hydrogen embrittlement. In this study, the deformation and fracture behaviors of high hydrogen 7xxx alloys containing 0.0% Mn and 0.6% Mn are observed in situ using synchrotron radiation X-ray tomography. Although no significant differences appear between the two alloys regarding the initiation of quasicleavage cracks, the area fractions of final quasicleavage fractures are 16.5% and 1.0% for 0.0%Mn and 0.6%Mn alloys, respectively; this finding indicates that Mn addition reduces hydrogen-induced fractures. The obtained macroscopic hydrogen embrittlement is quantitatively analyzed based on hydrogen partitioning in alloys. Adding 0.6% Mn, generating second-phase particles with high hydrogen trapping abilities, significantly suppresses hydrogen-induced quasicleavage fracture. The results of an original hydrogen partitioning analysis show that the dispersion of Mn-based particles ($Al_{12}Mn_3Si$) with high hydrogen trapping abilities reduces the hydrogen concentration at the semicoherent $MgZn_2$ interface and suppresses hydrogen embrittlement.

KEYWORDS: *Aluminum alloy, Hydrogen, Hydrogen embrittlement, Hydrogen-induced cracking, Fracture mechanics, Microstructure.*

1 INTRODUCTION

Al-Zn-Mg-Cu (7xxx) alloys are well-known high-strength aluminum alloys; as their strength increases with increasing Zn and Mg contents, their susceptibility to hydrogen embrittlement increases accordingly [1–4]. We have previously proposed that this phenomenon occurs due to hydrogen-induced precipitate interface debonding; this process is caused by hydrogen accumulation at the interface between the matrix and the $MgZn_2$ precipitate [5]. $MgZn_2$, which is a precipitate called the η-phase, is responsible for Al-Zn-Mg alloy precipitation strengthening, and it simultaneously triggers hydrogen-induced quasicleavage fracture. As a remedy for this fracture, a strategy has been proposed to partition hydrogen to the interior of the second-phase particles rather than the precipitate interface; the second-phase particles are innocuous for hydrogen embrittlement. The second-phase particles must have an internal hydrogen trapping energy equal to or greater than that of the $MgZn_2$ precipitate interface (0.55 eV/atom at maximum [6–9]). Specifically, Al_7Cu_2Fe particles with internal hydrogen trapping energies of 0.56 eV/atom are considered attractive [10]. However, our investigation has revealed that while Al_7Cu_2Fe particles have high hydrogen trapping energies, they have lower ductilities and poorer mechanical properties than the matrix, damaging the particles and causing premature fracture in aluminum alloys [9,11].

To prevent hydrogen embrittlement by second-phase particles, it is imperative to explore other particles that are less susceptible to damage during deformation with higher hydrogen trapping energies. We find that some Mn-based particles among the second-phase particles have high hydrogen trapping energies and can be dispersed more finely than Al_7Cu_2Fe, thus contributing to hydrogen embrittlement prevention in Al-Zn-Mg alloys. However, this investigation results from using high-purity alloys cast in laboratories. The chemical compositions and crystal structures of Mn-based particles dispersed in practical 7xxx alloys are complicated; on this basis, the particle hydrogen partitioning behaviors are not deterministic. The addition of Mn has been implemented as a strategy to develop new 7xxx alloys that combine high resistance to environmental degradation with high strength without sacrificing ductility [12–14]. Mn has been found to facilitate the production of 7xxx aluminum alloys with high resistance to environmentally assisted cracking in combination with appropriate amounts of Zn, Mg, and Cu. Furthermore, it has been established that the addition of Mn to an Al-Zn-Mg-Cu alloy without others (e.g., Cu, Cr) is insufficient to suppress environment-induced cracking. Alcoa registered an alloy X7080 (containing 5-7%Zn + 1.5-3%Mg + 0.5-1.5%Cu + 0.1-0.7%Mn) that was immediately withdrawn due to SCC problems in 1965 [1].

The above suggests that in 7xxx alloys with Mn addition, the complex composition of second-phase particles containing Mn can influence hydrogen embrittlement and stress corrosion cracking. In this study, we clarify the influences of Mn-based second-phase particles on hydrogen-related fracture behaviors in practical 7xxx alloys. For this purpose, the deformation and fracture processes of hydrogen-charged 7xxx alloys are observed in situ by synchrotron X-ray chromatography (CT). The hydrogen embrittlement behavior and hydrogen partitioning of the material to the second-phase particles are then analyzed to demonstrate the abilities of Mn-based particles to suppress hydrogen embrittlement.

2 EXPERIMENT

2.1 Materials

Two different alloys were used in this study based on the 7xxx series (Al-Zn-Mg-Cu) alloy: one with and one without a 0.6 mass% Mn addition. The chemical compositions of the alloys are shown in Table 1. The alloy with Mn addition was the 0.6Mn alloy, and the alloy without Mn addition was the 0.0Mn alloy. After casting, the alloy was homogenized (743 K; 10 h), hot rolled (673 K), solution treated (743 K; 2 h), quenched, and subjected to natural aging (room temperature; 24 h) and artificial aging (393 K; 24 h). This aging state was peak aging. The alloy after heat treatment was cut into the specimen geometry shown in Fig. 1 by wire-cut electrical discharge machining in water. This underwater wire-cut process was used for cutting the specimens and for hydrogen charging; several mass ppm of hydrogen could be charged into aluminum alloys [3,15]. The surface of the specimens exhibits a significant hydrogen content after EDM. The specimens were preserved in acetone for nearly four days to facilitate the diffusion of hydrogen into the interior of the specimens. The estimated diffusion distance after four days was 2.8 mm, assuming a hydrogen diffusion coefficient of 2.3×10^{-11} m^2/s in aluminum at room temperature [16]. This diffusion distance surpasses the specimen size, and it is postulated that hydrogen diffuses from the surface to the center of the specimens.

2.2 Characterization

To measure the amount of internal hydrogen in the hydrogen-charged alloys, a thermal desorption analysis (TDA) apparatus with a gas chromatograph-type detector (PDHA-1000, NISSHA FIS, Inc.) was utilized. Hydrogen desorption was measured while continuously heating the specimen from room temperature to 773 K at an Ar flow rate of 20 mL/min and a temperature elevation rate of 1.5 K/min.

Micron-sized second-phase particles and fracture surfaces after in situ testing were observed using a JEOL JSM-7001F scanning electron microscope (SEM) at an acceleration voltage of 15 kV. Using the same SEM and acceleration voltage, crystal structure analysis by electron beam backscattered diffraction with a 3 µm step size (EBSD, Oxford Instruments Nordlys Nano & Aztec) was performed. Furthermore, a JEOL ARM-200F transmission electron microscope (TEM) equipped with energy dispersive spectroscopy (EDS) and a high-angle annular dark field (HAADF) detector was applied to observe the second-phase particles at an accelerating voltage of 200 kV. The electron probe size used in high-angle annular dark-field scanning transmission electron microscopy (HAADF-STEM) was approximately 0.3 nm to achieve relatively accurate atomic number (Z) contrast images.[17]. The specimens for transmission electron microscopy (TEM) observation were prepared using the Ar ion beam milling technique (PIPS) provided by Gatan Inc.

2.3 In situ *tensile test via synchrotron X-ray tomography*

To examine the deformation and fracture characteristics of the alloys, a projection-type synchrotron X-ray computed tomography (CT) was carried out using the BL20XU undulator beamline at SPring-8. A liquid nitrogen-cooled Si (111) double crystal monochromator was employed to produce a monochromatic X-ray of 20 keV. The imaging system was equipped with a CMOS camera (ORCA Flash 4.0 with 2048 x 2048 pixels, supplied by Hamamatsu Photonics K.K.), a GAGG single-crystal scintillator, and an optical lens. Each scan recorded 1800 projections, acquired through a 180° rotation with 0.1-degree increments. These projections were reconstructed into a three-dimensional image using a convolution backprojection algorithm [18]. The effective pixel size of the detector was 0.5 µm. The distance from the sample to the detector was 20 mm. In situ tensile tests were performed using an in situ testing machine (CT500, supplied by Deben UK, Ltd) at a displacement rate of 0.02 mm/min. In situ tensile tests were performed at room temperature, with no artificial control of humidity. At each step, the displacement was held for a period of 55.6 minutes prior to the next scan. This allowed hydrogen to redistribute without significant hydrogen loss. Tomographic images were acquired at each step with a displacement increment of approximately 0.02 mm (corresponding to an applied strain of 2-3%).

2.4 Tomographic image analysis

Microstructural parameters, such as the volume, surface area, and diameter, of each particle and pore were calculated using a marching cubes algorithm [19]. Only pores and particles that exceeded 9 voxels in volume were considered microstructural features in this study to reduce inaccuracies due to image noise. Precise image registration was performed to minimize the physical distances between identical particles imaged at adjacent loading steps. A microstructural tracking technique [20], which facilitated deformation behavior visualizations, was applied by tracking all particles throughout the deformation process. In addition, high-density 3D plastic strain mapping was performed by calculating the physical displacements of identical particles under different loading steps. Additional information on microstructure tracking and 3D strain mapping is provided elsewhere[20].

3 CHANGES IN HYDROGEN EMBRITTLEMENT BEHAVIORS BY TRACE Mn

Hydrogen desorption curves measured by TDA for 0.0 Mn and 0.6 Mn alloys after hydrogen charging by electrical discharge machining are shown in Fig. 2. An overview of the obtained TDA curves shows that no significant changes in the behaviors of the observed hydrogen desorption curves appear with or without Mn. However, as discussed in Chapter 4, some Mn-based particles are hydrogen trapping sites; intrinsically, the presence of Mn particles may influence hydrogen trapping in the alloy. The TDA curves of aluminum alloys, unlike those of steels, are often complex [21–24]. This phenomenon occurs due to the microstructural changes during TDA heating and the associated changes in hydrogen trapping [25]. Between room temperature and 773 K, the precipitates coarsen and then dissolve into the matrix. In addition, the characteristics of vacancy concentration, dislocation density, pores and particles change, and grain recrystallization occurs. These areas are the hydrogen trapping sites of aluminum [10,26–30], and the inevitable overlap of changes in the trapping sites with the thermally induced hydrogen desorption from the trapping sites poses severe challenges for the interpretation of the TDA curves for aluminum. The integrated amounts of intrinsic hydrogen are 3.00 mass ppm for the 0.6Mn alloy and 2.80 mass ppm for the 0.0Mn alloy; these values are nearly the same. As shown in Fig. 2, the maximum heating temperature of TDA is set at 773 K to avoid melting the specimens during measurement. Although the hydrogen in the specimens is not completely released during heating to the maximum temperature (773 K), the total amount of hydrogen released in one TDA is defined as the hydrogen concentration in the specimen in this study.

Fig. 3 shows the results of EBSD analysis of the 0.0Mn and 0.6Mn alloys. The inverse pole figure (IPF) maps shown in Fig. 3 (a) and (b) indicate that the two alloys have slightly different grain orientations; however, the grain-size distribution is almost the same as that shown in Fig. 3(c). While Mn is known to have a grain refinement effect, the effect is stronger with Zr. Therefore, the grain size was similar with and without Mn addition. It is reasonably difficult to speculate that the effect of Mn addition did not appear in grain size but only in orientation. The difference in orientation direction is probably not due to the effect of Mn addition but to the different cutting positions of the small specimens (0.6 mm thick) for the synchrotron experiment. The distance from the surface of the rolled plate differs depending on the cutting position of the specimen, which may have resulted in a slight difference in the orientation direction.

Fig. 4 shows nominal stress–nominal strain curves obtained from synchrotron X-ray CT in situ tensile tests of 0.0Mn and 0.6Mn alloys. The tensile strength of the 0.6Mn alloy was 71 MPa higher than that of the 0.0Mn alloy. It has been well documented in 7xxx series alloys that Mn additions form dispersoids of less than 1 μm, thereby increasing the strength, and the results of Fig. 4 are also consistent with this [13,14,31,32]. The maximum stress in the 0.6Mn alloy increases as a result of solid solution strengthening by solute Mn and dispersion strengthening by Mn particles. The fracture strains of the 0.0Mn and 0.6Mn alloys are 13.6% and 12.7%, respectively, which are comparable. Fig. 5 shows the fractographs after the tensile test observed using SEM. In the 0.0 Mn alloy shown in Figs. 5(a) and 5(c), quasicleavage fracture is observed in the near-surface region, and the area fraction of quasicleavage fracture is 16.5%. The 0.6 Mn alloy shown in Figs. 5(b) and 5(d) shows almost no quasicleavage fracture relative to the 0.0 Mn alloy; the area fraction of quasicleavage fracture is 1.0%, and it is limited to the corners of the fracture surface. The addition of 0.6% Mn greatly decreases quasicleavage fracture and suppresses the macroscopic hydrogen-induced degradation of mechanical properties in the alloy. The stress–strain curves shown in Fig. 4 indicate that the 0.0Mn alloy has a slightly higher fracture strain than the 0.6Mn alloy; however, simultaneously, the 0.0Mn alloy has a stronger tendency toward quasicleavage fracture. In other words, the 0.6Mn alloy showed an increase in tensile strength and a slight decrease in ductility. This is a typical strength-ductility balance of increased strength accompanied by decreased ductility and is not due to hydrogen embrittlement, as shown by the brittle fracture coverage in Fig. 5(b).

Synchrotron X-ray imaging can clearly visualize whether the crack initiation site is on the surface or inside. Crack initiation sites in 7XXX and ternary Al-Zn-Mg alloys were on the surface in this experiment and in all other previous experiments [7,15,33]. In this study, hydrogen is charged by EDM in water after aging, as described in section 2.1. The specimens were stored at room temperature for approximately 4 days to allow the charged hydrogen to diffuse into the interior of the specimen before experiments. However, even after 4 days, the hydrogen concentration on the surface probably remains higher than that of the interior. In addition, hydrogen originating from the reaction between atmospheric moisture and the aluminum surface during deformation increased the hydrogen concentration on the surface. As a result, hydrogen-induced brittle cracks initiate from the surface due to the high hydrogen concentration during deformation.

Fig. 6 shows the results of mapping the plastic strain at each strain stage for the 0.0Mn and 0.6Mn alloys by a local plastic strain analysis associated with the particle tracking described in the experimental method [20]. Fig. 6 shows a two-dimensional virtual cross-section that corresponds to the location of the red dashed line on the fracture surfaces in Fig. 5(a) and (b), i.e., the cross-section where quasicleavage cracking occurs. In the

0.0Mn alloy, the strain distribution is homogeneous at an applied strain of 2.2% (Fig. 6(a)); a quasicleavage crack initiates at an applied strain of 5.6% (Fig. 6(b)), propagating with wide strain localization extending from the crack tip (Fig. 6(c)). The fracture initiation point is a quasicleavage crack occurring at an applied strain of 5.6%. This strain localization over several hundred μm at the crack tip has been reported previously [3]. Bhuiyan *et al*. performed a local strain analysis similar to our analysis for 7xxx aluminum alloys. The researchers discussed the combined effect of tensile stress and a high concentration of hydrogen in front of the crack tip to reduce the local flow stress and localizing slip. In the 0.6Mn alloy, the final fracture path and strain localization are significantly different from those of the 0.0Mn alloy; however, the behaviors of uniform deformation (2.2% applied strain in Fig. 6(d)) and the formation of quasicleavage cracks (7.7% applied strain in Fig. 6(e)) are not substantially different from those of the 0.0Mn alloy. In the 0.6Mn alloy, as shown in Fig. 6(f), strain localization occurs in the form of a shear band in the direction of approximately 45 degrees just before fracture; the final fracture surface is developed along this direction. Although the fracture path originates from the initial quasicleavage crack, as shown in Fig. 5(b), quasicleavage crack propagation is limited; ductile fracture with shear band formation is the dominant fracture mode. Lee *et al.* performed mechanical tests and TEM observations of Al-Zn-Mg(-Mn) alloys and concluded that Mn dispersoids act as a barrier to dislocation motion and promote cross-slip with uniform deformation [13]. As discussed later, Mn-based dispersions were also formed in the 0.6Mn alloy in this study, which may have affected strain localization in regions where the cracks did not propagate (Fig. 6(f)).

Based on the analysis of local plastic strain just before fracture shown in Fig. 6, we estimate the vacancy concentrations, C_v, the density of geometrically necessary dislocations (GNDs), ρ_GND, and the density of statistically stored dislocations (SSDs), ρ_SSD, during deformation. The vacancy concentration and dislocation density, $\rho_\mathrm{dis.}$, values as functions of elemental strain are provided by the following equations [7,15,34–37].

$$C_\mathrm{v} = \chi \frac{\sigma \Omega_0}{Q_\mathrm{f}} \varepsilon_\mathrm{true} + C_0 \tag{1}$$

$$\rho_\mathrm{dis.} = \rho_\mathrm{GND} + \rho_\mathrm{SSD} = \bar{r}\frac{\eta^\mathrm{p}}{b} + \frac{\sqrt{3}\varepsilon_p}{bl} \tag{2}$$

where $\chi = 0.1$, σ is the flow stress, $\varepsilon_\mathrm{true}$ is the true strain, Q_f is the energy of vacancy formation, Ω_0 is the atomic volume of aluminum, C_0 is the initial vacancy concentration, $\bar{r}$ is the Nye factor, η^p is the plastic strain gradient, b is the Burgers vector, ε_p is the equivalent plastic strain, and l is the mean free path. SSD accumulates by randomly trapping other dislocations, whereas GND is required for the compatible deformation of different parts of a material [38]. Figs. 7(a), (b), and (c) show maps of vacancy concentration, GND and SSD density for the 0.6Mn alloy at 10.7% applied strain, respectively. The vacancy concentrations and SSD densities are condensed in regions of high plastic strain, and the GND density is locally high in regions where the change in equivalent plastic strain is large. Hydrogen in the material is not uniformly distributed, and it is partitioned among various hydrogen trapping sites, such as vacancies and dislocations. This analysis, which allows the local analysis of vacancy concentration and the dislocation density after deformation, is valuable for characterizing hydrogen partitioning in materials, given that vacancy formation and dislocation multiplication occur during tensile deformation. The results of Fig. 7 are used as analytical parameters for hydrogen partitioning in the alloy as the quantified hydrogen trapping site density, as discussed later in Section 5.5.

4 INTERNAL HYDROGEN TRAPPING OF DISPERSED Mn PARTICLES

The formation of Mn-based second-phase particles of various compositions has been reported by adding trace amounts of Mn to aluminum alloys [39–42]. To understand the suppression of hydrogen-induced quasicleavage fracture by 0.6% Mn addition, an evaluation of the influence of Mn addition on particle formation is important. More specifically, hydrogen can be trapped inside the formed Mn-based particles, as reported for

Al_7Cu_2Fe [10]. Therefore, Mn-based particles are identified by analyzing the second-phase particles in the alloys used in this study by using SEM and TEM; the hydrogen trapping energies inside these particles are derived by density functional theory (DFT) calculations.

First, SEM and HAADF-STEM observations of the 0.0Mn and 0.6Mn alloy microstructures are performed. The microstructure observed in the 0.0Mn alloy using SEM is shown in Fig. 8(a). The composition of the 0.0Mn alloy is the same as that previously reported [3,43], and the second-phase particles dispersed in the matrix are Mg_2Si and Al_7Cu_2Fe on the order of a few μm. Mg_2Si has no internal hydrogen trapping sites, and Al_7Cu_2Fe has 0.56 eV/atom internal hydrogen trapping sites [10]. Figs. 8(b) and 8(c) show the HAADF-STEM images of 0.0Mn alloys. Fig. 8(b) shows that a fully coherent η' phase and an Al_3Zr phase are precipitated in the matrix, and Fig. 8(c) shows that a slightly coarser η_2 phase (disc shape) than η' is precipitated, which has a coherent interface on the plate face and a semicoherent interface on the edge face. As mentioned in the introduction, the coherent and semicoherent interfaces of $MgZn_2$ (η' and η_2 phases) are hydrogen trapping sites with a maximum trapping energy of 0.55 eV/atom. Al_3Zr has hydrogen trap sites inside the phase, which were judged to be negligible in this study because the trap energy is as low as 0.12 eV/atom[8] and the precipitation density is not high. Fig. 9 shows the SEM backscattered electron images, HAADF–STEM images and scanning transmission electron microscopy–energy dispersive X-ray spectroscopy (STEM–EDS) maps of the 0.6Mn alloy. The backscattered electron image in Fig. 9(a) shows coarse second-phase particles on the order of several microns, which are not observed for 0.0Mn. A point analysis of these particles by scanning electron microscopy–energy dispersive X-ray spectroscopy (SEM–EDS) shows compositions of 74.0% Al, 9.1% Fe, 6.3% Mn, 4.7% Si, 2.7% Cu, 2.2% Zn, and 1.1% Mg (in mol%). Since the signals from the matrix are unavoidably mixed in the characteristic X-rays detected by SEM–EDS, the composition of these Mn-based particles is $Al_{12}(Fe, Mn)_3Si$. In addition, Fig. 9(a) shows that the 0.6Mn material has finer second-phase particles dispersed in the matrix than $Al_{12}(Fe, Mn)_3Si$ [44–46]. Fig. 9(b) shows the HAADF–STEM image of these fine particles, and Fig. 9(c)~(i) shows the STEM–EDS elemental maps. The STEM–EDS point analysis shows that the composition of this fine particle is 76.95% Al, 1.53% Mg, 5.69% Cu, 11.27% Mn, and 4.09% Zn (in mol%). Based on the obtained Cu and Mn atomic concentration ratios and the particle compositions reported for Mn-added 7xxx aluminum alloys, this submicron-order Mn-based particle is $Al_{20}Cu_2Mn_3$ [41,42]. For the 0.6Mn alloy, we did not perform HAADF-STEM observations at high magnification, as shown in Figs. 8(b) and 8(c). This is because the diffusion coefficient of Mn in aluminum is significantly lower than that of Zn and Mg[47], and the influence of $MgZn_2$ precipitation was judged to be poor.

Next, the internal hydrogen trapping energies of the identified Mn-based particles are derived by DFT calculations (Vienna Ab initio Simulation Package (VASP)) [48–50]. Fig. 10(a), (b), and (c) show the unit cell models of $Al_{20}Cu_2Mn_3$ (space group: Cmcm), $Al_{12}Fe_3Si$ (space group: Pm-3) and $Al_{12}Mn_3Si$ (space group: Pm-3), respectively (all models are described by Visualization for Electronic Structural Analysis (VESTA) software) [51]. By using these crystal models, the internal hydrogen trapping energies of the interstitial sites of each particle are comprehensively explored through VASP. The compositions of the coarse Mn particles identified in the 0.6Mn alloy are $Al_{12}(Fe, Mn)_3Si$; however, the atomic configuration cannot be uniquely identified because Fe and Mn atoms are positioned in substitution-type sites. Therefore, we explore hydrogen trapping sites in both $Al_{12}Fe_3Si$ and $Al_{12}Fe_3Si$. The principles of the exploration of hydrogen trapping sites and energies inside the particles are as follows, as in a previous report [10]. Voronoi tessellation analysis shows possible interstitial sites in the crystals, as shown in Fig. 10(a)~(c). The vertex of the Voronoi polyhedron is a possible trap site for a hydrogen atom. In addition, the center point of each plane on the Voronoi polyhedron is a possible trap site. In our method, the definition of the inherently negative trapping energy (E_{trap}) is the energy change by the migration of dissolved hydrogen atoms from a tetrahedral site in the aluminum matrix to a possible trapping site in the perfect crystal of a particle. The following equation is shown:

$$E_{\mathrm{trap}} = E_{\mathrm{tot}}(\mathrm{H} + \mathrm{particle}) - E_{\mathrm{tot}}(\mathrm{particle}) - \{E_{\mathrm{tot}}(\mathrm{H} + \mathrm{Al}) - E_{\mathrm{tot}}(\mathrm{Al})\} \tag{3}$$

where the total energy of the unit cell, E_{tot}, is calculated from the ab initio simulation using VASP. A Monkhorst-Pack algorithm is selected for the Brillouin-zone k-point samplings [52]. A plane-wave energy cutoff of 360 eV is used with a first-order Methfessel-Paxton smearing scheme, employing a smearing parameter of 0.2 eV. The total energy converges to 10^{-6} eV in all the calculations. In this study, the calculated trapping energy, E_{trap}, is an inherently negative value. However, the trapping energy is usually referred to as a positive value ($-E_{\mathrm{trap}}$). The zero point energy (ZPE) of hydrogen is not considered in the DFT calculation of hydrogen trapping energies in this study. The ZPE of hydrogen is in the range of 0.11-0.20 eV/atom. At the tetrahedral site in the aluminum lattice, the hydrogen ZPE is approximately 0.16 eV/atom [53]. Therefore, the correction energy of the ZPE is within 0.05 eV/atom, which is smaller than the obtained trapping energies.

The strongest hydrogen trapping sites for each calculated particle are shown neighboring each crystal model in Fig. 10(a)~(c) and are hexahedral sites with two Mn atoms and three Al atoms at the vertices for $Al_{20}Cu_2Mn_3$; additionally, there are tetrahedral sites with four Al atoms at the vertices for $Al_{12}Fe_3Si$ and $Al_{12}Mn_3Si$. The sites are tetrahedral with one Mn atom and three Al atoms at the vertices. The hydrogen trapping energies, $-E_{\mathrm{trap}}$, at these sites are 0.24, 0.36, and 0.66 eV/atom for $Al_{20}Cu_2Mn_3$, $Al_{12}Fe_3Si$, and $Al_{12}Mn_3Si$, respectively. The three crystals shown in Fig. 10(a)~(c) exhibit crystallographic symmetry, and the strongest hydrogen trap site has multiple crystallographically equivalent sites within the unit cell. We have calculated multiple hydrogen trapping at these sites, which are shown in Fig. 10(d). Fig. 10(d) shows that there are eight strong hydrogen trap sites in the unit cell for $Al_{12}Fe_3Si$ and that hydrogen is stably trapped in four of these sites. Similarly, in $Al_{12}Fe_3Si$ and $Al_{12}Mn_3Si$, there are 6 and 24 equivalent strongest hydrogen traps in the unit cell, providing stable multiple trapping of 6 and 12 hydrogen, respectively. This finding suggests that $Al_{12}Mn_3Si$ is the most hydrogen-trapping particle among these three second-phase particles, exhibiting a hydrogen trapping energy of 0.66 eV/atom and a trapping site density of 12 atomH/cell.

In our calculations, we employed several simplifying assumptions to minimize computational complexity. Initially, we assumed that the crystal structures of $Al_{20}Cu_2Mn_3$, $Al_{12}Fe_3Si$ and $Al_{12}Mn_3Si$ were completely stoichiometric. However, it remains uncertain whether the second phase particles in the aluminum matrix have near-stoichiometric crystal structures. Additionally, we assumed the absence of any crystallographic defects in these compounds. While vacancy-type defects could potentially serve as stable sites for hydrogen, for simplicity, we did not consider such defects. Despite utilizing the Voronoi tessellation technique to identify potential hydrogen trap sites, it cannot be ruled out that some sites may have been missed. Nonetheless, given the constraints on computation time, this approach is considered practical at present.

5 HYDROGEN PARTITIONING BEHAVIOR

Hydrogen in the alloy is partitioned to each site [54]. We quantitatively estimated the hydrogen partitioning into each hydrogen trap in the alloys used. The following relationship is established between the total amount of hydrogen in the alloy, C_{tot}, the hydrogen trapped in the lattice, C_{L}, and the hydrogen trapped in the other sites, $C_{\mathrm{T}i}$ [7,15,55].

$$C_{\mathrm{tot}} = C_{\mathrm{L}} + \sum C_{\mathrm{T}i} + C_{\mathrm{pore}} = \theta_{\mathrm{L}} N_{\mathrm{L}} + \sum \theta_{\mathrm{T}_i} N_{\mathrm{T}_i} + 2N_A \frac{4\gamma V}{dRT} \tag{4}$$

where C_{pore} is the amount of hydrogen trapped inside the pores, ϑ_{L} is the hydrogen occupancy of the lattice site (t-site), $\vartheta_{\mathrm{T}i}$ is the hydrogen occupancy of trapping site i, N_{L} is the trapping site density of the lattice, $N_{\mathrm{T}i}$ is the density of trapping site i, N_{A} is the Avogadro constant, V is the total volume of the pores, d is the average diameter of the pores, γ is the surface energy of aluminum in the presence of hydrogen [30], R is the gas constant and T is the temperature. The key parameters for solving the hydrogen partitioning model in Equation (4) are hydrogen occupancies and trap site densities. The following Oriani's equation is established in local thermal equilibrium for the hydrogen occupancy between the lattices at each trap site.

$$\frac{\theta_{\mathrm{T}_i}}{1-\theta_{\mathrm{T}_i}} = \theta_{\mathrm{L}} \exp\left(\frac{E_{\mathrm{trap\_}i}}{RT}\right) \tag{5}$$

where $E_{\mathrm{trap\_}i}$ is the hydrogen trapping energy for each hydrogen site; the hydrogen trapping energies for the sites considered in this study, which are calculated by DFT calculations, are listed in Table 2. The hydrogen trapping site density, N_{Ti}, is measured by various experiments. The vacancy concentration and dislocation density are quantified based on local plastic strain components, as shown in Fig. 7; the sizes and volume fractions of second-phase particles and pores are quantified by synchrotron X-ray CT. Grain boundaries and $MgZn_2$ precipitates are quantified by optical microscopy and HAADF–STEM, respectively, the details of which are shown in previous reports [7–9,15].

Fig. 11 shows the results of the analysis of hydrogen partitioning in 0.0 Mn and 0.6 Mn alloys. The analysis results are for the strain stage prior to fracture, where Fig. 11(a) is the total hydrogen partitioned to each trap site and Fig. 11(b) is the hydrogen occupancy of each trap site. Comparing the results for 0.0Mn and 0.6Mn placed in Fig. 11(a), the highest amount of hydrogen was trapped at the $MgZn_2$ semicoherent interface for the 0.0Mn alloy and at the IMC particles ($Al_{12}(Fe, Mn)_3Si$) for the 0.6Mn alloy. As shown in Fig. 1, the total hydrogen content in the alloy is not significantly changed by the addition of Mn. In the 0.6Mn alloys, the partitioning of hydrogen into second-phase particles formed by the addition of Mn resulted in a relative decrease in the amount of trapped hydrogen at the $MgZn_2$ semicoherent interface, which led to hydrogen-induced quasicleavage fractures. This phenomenon occurs because, as shown in Table 2, $Al_{12}Mn_3Si$ in the 0.6Mn alloy has a higher hydrogen trapping energy (0. 66 eV/atom) than that of the $MgZn_2$ semicoherent interface (0.55 eV/atom). The behavior of hydrogen occupancy shown in Fig. 11(b) is similar to that of the trapped hydrogen content, where the hydrogen occupancy of second-phase particles in the 0.6 Mn alloy was higher than that at the $MgZn_2$ semicoherent interface. The reported mechanisms of hydrogen-induced quasicleavage fracture include the formation of hydrogen-vacancy complexes associated with vacancy stabilization by hydrogen, the formation of hydrogen-induced nanovoids, and hydrogen-dislocation interactions [56–61]. However, as shown in Fig. 11(a), the hydrogen trapped in vacancies and dislocations is several orders of magnitude less than that trapped in $MgZn_2$. Nagumo *et al.* discovered that hydrogen trapped at vacancies stabilizes the vacancies and induces the initiation of nanovoids [62,63]. Su *et al.* found that nanovoids induced by hydrogen in Al-Zn-Mg-Cu aluminum alloys form uniformly in the region of strain localization. Furthermore, the growth or merging of nanovoids caused by hydrogen is not seen even before fracture, suggesting that nanovoids do not play a dominant role in inducing quasicleavage cracks in Al-Zn-Mg-Cu aluminum alloys[2]. In addition, neither growth nor coalescence of hydrogen-induced nanovoids are observed even just before fracture, indicating that nanovoids do not behave as the dominant factor of hydrogen-induced quasicleavage cracks in Al-Zn-Mg-Cu aluminum alloys [64,65]. For grain boundaries, it has been reported that if large amounts of hydrogen are enriched at the aluminum grain boundary, hydrogen-induced debonding can occur, analogous to the precipitate interface [29]. However, the hydrogen trapping energies of the grain boundaries were low, below 0.27 eV/atom, even for $\Sigma9(221)$ and $\Sigma5(012)$, where grain boundary energies are high, indicating that the trapped hydrogen at the grain boundaries was more than five orders of magnitude lower than that at the semicoherent interface of $MgZn_2$. It is reasonably inconceivable that dilute hydrogen trapped in these vacancies, dislocations and grain boundaries dominates the hydrogen embrittlement of aluminum. We propose trapped hydrogen at the $MgZn_2$ precipitate interface and its debonding as the mechanism of hydrogen-induced quasicleavage fracture in Al-Zn-Mg alloys.

Whether hydrogen trapping of particles is positive or detrimental to material failure depends on the hydrogen trapping sites of particles and related phenomena induced by hydrogen trapping. In $MgZn_2$, there are no internal hydrogen trap sites. The coherent and semicoherent interfaces are hydrogen trap sites, and this interfacial hydrogen induces the debonding of $MgZn_2$ interfaces, resulting in macroscopic hydrogen embrittlement [5]. Thus, hydrogen trapping at the $MgZn_2$ interfaces is detrimental. $Al_{12}(Fe, Mn)_3Si$, investigated in this study, and Al_7Cu_2Fe [10] have internal hydrogen trap sites, and their trap energy is higher than that of $MgZn_2$, which causes hydrogen embrittlement. Therefore, hydrogen is preferentially partitioned inside these particles rather than at the $MgZn_2$ interface, which contributes to the prevention of hydrogen embrittlement. Therefore, in alloys with dispersed $Al_{12}(Fe, Mn)_3Si$ or Al_7Cu_2Fe particles, hydrogen is preferentially partitioned inside these particles rather than at the $MgZn_2$ interface, thereby suppressing hydrogen embrittlement. On fracture surfaces, hydrogen-induced quasicleavage and intergranular fractures are decreased, and the fraction of dimpled fracture is increased, as shown in Fig. 5.

The dispersion of second-phase particles, which have high hydrogen trapping ability, reduced the trapped hydrogen concentration at the $MgZn_2$ precipitate interface and suppressed quasicleavage fracture, as shown in Fig. 5(b). On the other hand, it is evident that even though Mn-based second-phase particles were dispersed, a slight quasicleavage fracture appeared. As shown in Fig. 10, the Mn-based particles exhibiting high hydrogen trapping energy were not fine and densely dispersed $Al_{20}Cu_2Mn_3$ but $Al_{12}(Fe, Mn)_3Si$ on the order of a few micrometers. In the region where the dispersion of $Al_{12}(Fe, Mn)_3Si$ is locally coarse, the hydrogen concentration at the $MgZn_2$ interface is considered to be high, resulting in quasicleavage cracking. This finding suggests that to develop aluminum alloys with high resistance to hydrogen embrittlement by dispersing IMC particles, it is crucial not only to focus on the high hydrogen trapping energy of second-phase particles but also on the high density and fine dispersion of the relevant particles. A comprehensive interpretation of which crystalline structures and chemical compositions of second-phase particles trap hydrogen more strongly is not available at present. Based on the report of Xu *et al*. and the results of this study [8], particles composed of ternary or more components and having a complex crystal structure show a strong tendency for hydrogen trapping; however, there are exceptions such as $Al_{20}Cu_2Mn_3$, which need further investigation.

Finally, the influences of holding time in synchrotron in situ tensile tests on hydrogen embrittlement are discussed. Bhuiyan *et al.* reported an increase in the area fraction of quasicleavage fracture when the holding time was increased from 0 to 2.1 ks for the 0.0Mn alloy used in this study, as shown in Fig. 12 [3]. Fig. 12 also shows the results for the 0.6Mn alloys used in this study at holding times of 0, 0.83, and 3.3 ks. In the 0.0Mn alloy, quasicleavage fracture increases significantly with increasing holding time, whereas the increase in quasicleavage fracture with increasing holding time is limited in the 0.6Mn alloy. Holding time is a parameter that can be considered equivalent to the strain rate in slow strain rate tensile testing, and the effect of increased holding time is interpreted as a decrease in the strain rate. Hydrogen repartitioning or hydrogen invasion from outside the specimen occurs during the tensile deformation process [65–67], making hydrogen embrittlement more pronounced at longer holding times (lower strain rates). This phenomenon occurs due to the complicated superposition of the formation of local stress gradients, changes in hydrogen trap site density due to loading, hydrogen diffusion during deformation, and hydrogen invasion caused by the fracture of the passive film on the aluminum surface. During holding, the annihilation of vacancies formed during deformation occurs, and the associated repartitioning of hydrogen also occurs. Vacancies are known to be stabilized by hydrogen and form nanovoids. In previous literature, we investigated the effects of the creation/annihilation of vacancies, nanovoid formation, and related deformation and fracture behavior[65]. We concluded that the nanovoid contribution to hydrogen embrittlement fracture is minor. Nanovoids can trap enormous quantities of hydrogen, functioning as major hydrogen trap sites in Al–Zn–Mg–Cu alloys.

The results in Fig. 12 suggest that a trace Mn addition of 0.6% is beneficial for the prevention of hydrogen embrittlement, considering not only the internal hydrogen charged before the test but also the hydrogen invasion and repartitioning during deformation. In other words, it is presumed that the Mn-based second-phase particles preferentially trap hydrogen during deformation rather than the $MgZn_2$ interface, thereby suppressing quasicleavage fracture. However, the extent to which hydrogen diffuses into micron-order second-phase particles at room temperature remains to be clarified, and further investigation is needed.

6 CONCLUSIONS

The dispersion of Mn-based second-phase particles was investigated as a novel approach to prevent 7xxx aluminum alloy hydrogen embrittlement. Alloys differing only in the presence or absence of trace additions of Mn were prepared, microstructural characterization was performed, and hydrogen embrittlement behavior was observed in situ using synchrotron radiation X-ray tomography. The prevention of hydrogen embrittlement by 0.6% Mn addition was then quantitatively analyzed based on hydrogen partitioning, and the following findings were obtained.

- The 0.6 Mn addition did not change the total trapped hydrogen content of the alloy but increased the maximum tensile strength of the alloy by approximately 100 MPa and slightly decreased the fracture strain in the holding-time test. The area fraction of the quasicleavage fracture of the 0.0 Mn and 0.6 Mn alloys after the holding time test were 16.5% and 1.0%, respectively, demonstrating that the addition of a small amount of Mn improved the hydrogen embrittlement.

- In the 0.6Mn alloy, $Al_{20}Cu_2Mn_3$ and $Al_{12}(Fe, Mn)_3Si$ were dispersed as Mn-based second-phase particles. Hydrogen trapping energies inside the particles of $Al_{20}Cu_2Mn_3$, $Al_{12}Fe_3Si$, and $Al_{12}Mn_3Si$ were explored by DFT calculations, and the strongest hydrogen trapping energies were 0.24, 0.36, and 0.66 eV/atom, respectively. The number of hydrogen traps in $Al_{12}Mn_3Si$ was greater than that in the $MgZn_2$ semicoherent interface (0.55 eV/atom).

- Hydrogen partitioning analysis showed that Mn-based second-phase particles formed in the 0.6Mn alloy trap a larger amount of hydrogen than the $MgZn_2$ semicoherent interface. This preferential hydrogen partitioning to Mn particles prevented quasicleavage fracture.

7 ACKNOWLEDGMENTS

This work was supported by JST CREST Grant Number JPMJCR 1995, Japan and JSPS KAKENH Grant Number 21K14037, Japan. This research was supported in part by a grant from both the Light Metal Educational Foundation, Japan, and Japan Aluminum Association, Japan. The synchrotron radiation experiments were performed at SPring-8 with the approval of the Japan Synchrotron Radiation Research Institute through proposal number 2020A1531/2021A1100/2021B1124. STEM measurements were supported by the “Advanced Research Infrastructure for Materials and Nanotechnology in Japan (ARIM)” of the Ministry of Education, Culture, Sports, Science and Technology (MEXT) through proposal number JPMXP1222OS0011.

8 REFERENCES

1. Holroyd, N.J.H., T.L. Burnett, J.J. Lewandowski, and G.M. Scamans, *Corrosion* 79 (2023): pp. 48–71.
2. Su, H., H. Toda, R. Masunaga, K. Shimizu, H. Gao, K. Sasaki, M.S. Bhuiyan, K. Uesugi, A. Takeuchi, and Y. Watanabe, *Acta Mater.* 159 (2018): pp. 332–343.
3. Bhuiyan, M.S., Y. Tada, H. Toda, S. Hang, K. Uesugi, A. Takeuchi, N. Sakaguchi, and Y. Watanabe, *Int. J. Fract.* 200 (2016): pp. 13–29.
4. Song, R.G.G., W. Dietzel, B.J.J. Zhang, W.J.J. Liu, M.K.K. Tseng, and A. Atrens, *Acta Mater.* 52 (2004): pp. 4727–4743.

5. Tsuru, T., K. Shimizu, M. Yamaguchi, M. Itakura, K. Ebihara, A. Bendo, K. Matsuda, and H. Toda, *Sci. Rep.* 10 (2020): pp. 1–8.
6. Shimizu, K., *Unpubl. Work* (n.d.).
7. Su, H., H. Toda, K. Shimizu, K. Uesugi, A. Takeuchi, and Y. Watanabe, *Acta Mater.* 176 (2019): pp. 96–108.
8. Xu, Y., H. Toda, K. Shimizu, Y. Wang, B. Gault, W. Li, K. Hirayama, H. Fujihara, X. Jin, A. Takeuchi, and M. Uesugi, *Acta Mater.* 236 (2022): p. 118110.
9. Wang, Y., H. Toda, Y. Xu, K. Shimizu, K. Hirayama, H. Fujihara, A. Takeuchi, and M. Uesugi, *Acta Mater.* 227 (2022): p. 117658.
10. Yamaguchi, M., T. Tsuru, K.I. Ebihara, M. Itakura, K. Matsuda, K. Shimizu, and H. Toda, *Mater. Trans.* 61 (2020): pp. 1907–1911.
11. Oikawa, R., K. Shimizu, Y. Kamada, H. Toda, H. Fujihara, M. Uesugi, and A. Takeuchi, *Mater. Trans.* (2022).
12. Boselli, J., G.H. Bray, C. Yanar, L.M. Karabin, S. Cambier, F.S. Bovard, and J.C. Lin, Improved Thick Wrought 7xxx Aluminum Alloys, and Methods for Making the Same, WO 2018/237196 A1, 2018.
13. Hee Lee, D., K. Cheol Kim, D. Seok Park, and S. Woo Nam, *Int. J. Fatigue* 21 (1999): pp. 383–391.
14. Park, D.S., and S.W. Nam, *J. Mater. Sci.* 30 (1995): pp. 1313–1320.
15. Shimizu, K., H. Toda, H. Fujihara, K. Hirayama, K. Uesugi, and A. Takeuchi, *Eng. Fract. Mech.* 216 (2019): p. 106503.
16. Young, G.A., and J.R. Scully, *Acta Mater.* 46 (1998): pp. 6337–6349.
17. Allen, L.J., S.D. Findlay, and M.P. Oxley, “Simulation and Interpretation of Images,” in Scanning Transm. Electron Microsc. (Springer, New York, NY, 2011), pp. 247–289.
18. Kak, A.C., and M. Slaney, *Principles of Computerized Tomographic Imaging* (Society for Industrial and Applied Mathematics, 2001).
19. Lorensen, W.E., H.E. Cline, W.E. Lorensen, and H.E. Cline, *Proc. 14th Annu. Conf. Comput. Graph. Interact. Tech. SIGGRAPH 1987* 21 (1987): pp. 163–169.
20. Kobayashi, M., H. Toda, Y. Kawai, T. Ohgaki, K. Uesugi, D.S. Wilkinson, T. Kobayashi, Y. Aoki, and M. Nakazawa, *Acta Mater.* 56 (2008): pp. 2167–2181.
21. Takahashi, J., K. Kawakami, and Y. Kobayashi, *Acta Mater.* 153 (2018): pp. 193–204.
22. Smith, S.W., and J.R. Scully, *Metall. Mater. Trans. A Phys. Metall. Mater. Sci.* 31 (2000): pp. 179–193.
23. Zhao, H., P. Chakraborty, D. Ponge, T. Hickel, B. Sun, C.H. Wu, B. Gault, and D. Raabe, *Nature* 602 (2022): pp. 437–441.
24. Chao, P., and R.A. Karnesky, *Mater. Sci. Eng. A* 658 (2016): pp. 422–428.
25. Nagumo, M., “Hydrogen Trapping and Its Detection,” in Fundam. Hydrog. Embrittlement (Springer, Singapore, 2016), pp. 11–33.
26. Ismer, L., M.S. Park, A. Janotti, and C.G. Van De Walle, *Phys. Rev. B - Condens. Matter Mater. Phys.* 80 (2009): pp. 1–10.
27. Yamaguchi, M., M. Itakura, T. Tsuru, and K.I. Ebihara, *Mater. Trans.* 62 (2021): pp. 582–589.
28. Izumi, T., and G. Itoh, *Mater. Trans.* 52 (2011): pp. 130–134.
29. Yamaguchi, M., K.I. Ebihara, M. Itakura, T. Tsuru, K. Matsuda, and H. Toda, *Comput. Mater. Sci.* 156 (2019): pp. 368–375.
30. Yamaguchi, M., T. Tsuru, K. Ebihara, and M. Itakura, *J. Japan Inst. Light Met.* 68 (2018): pp. 588–595.
31. Liu, S., J. Chen, W. Chai, Q. Wang, Z. Yang, L. Ye, and J. Tang, *Metall. Mater. Trans. A Phys. Metall. Mater. Sci.* 50 (2019): pp. 4877–4890.
32. Park, D.S., and S.W. Nam, *J. Mater. Sci. Lett.* 10 (1991): pp. 397–399.
33. Shimizu, K., H. Toda, K. Uesugi, and A. Takeuchi, *Metall. Mater. Trans. A Phys. Metall. Mater. Sci.* 51 (2020): pp. 1–19.
34. Militzer, M., W.P. Sun, and J.J. Jonas, *Acta Metall. Mater.* 42 (1994): pp. 133–141.
35. Deschamps, A., G. Fribourg, Y. Bréchet, J.L. Chemin, and C.R. Hutchinson, *Acta Mater.* 60 (2012): pp. 1905–1916.
36. Huang, Y., S. Qu, K.C. Hwang, M. Li, and H. Gao, *Int. J. Plast.* 20 (2004): pp. 753–782.
37. Brinckmann, S., T. Siegmund, and Y. Huang, *Int. J. Plast.* 22 (2006): pp. 1784–1797.
38. Ashby, M.F., *Philos. Mag.* 21 (1970): pp. 399–424.
39. Skolianos, S.M., T.Z. Kattamis, and O.F. Devereux, *Metall. Trans. A* 20 (1989): pp. 2499–2516.
40. Shuncai, W., L. Chunzhi, and Y. Minggao, *Mater. Res. Bull.* 24 (1989): pp. 1267–1270.
41. Chen, Z., P. Chen, and S. Li, *Mater. Sci. Eng. A* 532 (2012): pp. 606–609.
42. Shen, Z., C. Liu, Q. Ding, S. Wang, X. Wei, L. Chen, J. Li, and Z. Zhang, *J. Alloys Compd.* 601 (2014): pp. 25–30.
43. Su, H., S. Bhuiyan, H. Toda, K. Uesugi, A. Takeuchi, and Y. Watanabe, *Scr. Mater.* 135 (2017): pp. 19–23.

44. Ayer, R., J.Y. Koo, J.W. Steeds, and B.K. Park, *Metall. Trans. A* 16 (1985): pp. 1925–1936.

45. Mukhopadhyay, A.K., *Trans. Indian Inst. Met.* 62 (2009): pp. 113–122.

46. Mukhopadhyay, A.K., and A.K. Sharma, *Surf. Coatings Technol.* 92 (1997): pp. 212–220.

47. Du, Y., Y.A. Chang, B. Huang, W. Gong, Z. Jin, H. Xu, Z. Yuan, Y. Liu, Y. He, and F.Y. Xie, *Mater. Sci. Eng. A* 363 (2003): pp. 140–151.

48. Kresse, G., and J. Hafner, *Phys. Rev. B* 47 (1993): pp. 558–561.

49. Kresse, G., and J. Furthmüller, *Phys. Rev. B* 54 (1996): p. 11169.

50. Perdew, J.P., K. Burke, and M. Ernzerhof, *Phys. Rev. Lett.* 77 (1996): pp. 3865–3868.

51. Momma, K., F. Izumi, and IUCr, *Urn:Issn:0021-8898* 44 (2011): pp. 1272–1276.

52. Monkhorst, H.J., and J.D. Pack, *Phys. Rev. B* 13 (1976): p. 5188.

53. Wolverton, C., V. Ozoliņš, M. Asta, V. Ozoliņš, and M. Asta, *Phys. Rev. B - Condens. Matter Mater. Phys.* 69 (2004): p. 144109.

54. Scully, J.R., G.A. Young, and S.W. Smith, *Gaseous Hydrog. Embrittlement Mater. Energy Technol. Probl. Its Characterisation Eff. Part. Alloy Classes* (2012): pp. 707–768.

55. Toda, H., T. Hidaka, M. Kobayashi, K. Uesugi, A. Takeuchi, and K. Horikawa, *Acta Mater.* 57 (2009): pp. 2277–2290.

56. Birnbaum, H.K.K., C. Buckley, F. Zeides, E. Sirois, P. Rozenak, S. Spooner, and J.S.S. Lin, *J. Alloys Compd.* 253–254 (1997): pp. 260–264.

57. Li, S., Y. Li, Y.C. Lo, T. Neeraj, R. Srinivasan, X. Ding, J. Sun, L. Qi, P. Gumbsch, and J. Li, *Int. J. Plast.* 74 (2015): pp. 175–191.

58. Neeraj, T., and R. Srinivasan, *Corrosion* 73 (2017): pp. 437–447.

59. Martin, M.L., J.A. Fenske, G.S. Liu, P. Sofronis, and I.M. Robertson, *Acta Mater.* 59 (2011): pp. 1601–1606.

60. Deng, Y., and A. Barnoush, *Acta Mater.* 142 (2018): pp. 236–247.

61. Zhang, Z., G. Obasi, R. Morana, and M. Preuss, *Scr. Mater.* 140 (2017): pp. 40–44.

62. Nagumo, M., and M. Nagumo, 0836 (2017).

63. Nagumo, M., and K. Takai, *Acta Mater.* 165 (2019): pp. 722–733.

64. Gao, H., H. Su, K. Shimizu, C. Kadokawa, H. Toda, Y. Terada, K. Uesugi, and A. Takeuchi, *Mater. Trans.* 59 (2018): pp. 1532–1535.

65. Shimizu, K., H. Toda, C. Kadogawa, H. Fujihara, and A. Takeuchi, *Materialia* 11 (2020): p. 100667.

66. Nagao, A., M. Dadfarnia, B.P. Somerday, P. Sofronis, and R.O. Ritchie, *J. Mech. Phys. Solids* 112 (2018): pp. 403–430.

67. Horikawa, K., *Scr. Mater.* 199 (2021): p. 113853.

9 FIGURE CAPTIONS

FIGURE 1. Specimen geometry for the in situ tensile test in SPring-8.

FIGURE 2. TDA curves of prepared alloy with and without trace Mn to measure hydrogen content.

FIGURE 3. EBSD analysis of 0.0Mn and 0.6Mn alloys. (a) and (b) are the inverse pole figure maps for the nominal direction (ND) of 0.0Mn and 0.6Mn alloys, respectively. (c) Grain-size distribution.

FIGURE 4. Nominal stress–strain curves obtained from in situ tensile tests using synchrotron X-ray CT. The closed dots indicate the strain stages at which the CT scan was performed, where the decrease in stress corresponds to stress relaxation during the scan.

FIGURE 5. SEM fractographs of the alloy of (a) 0.0Mn, (b) 0.6Mn. The yellow masked area is the region of quasicleavage fracture. (c) and (d) are enlarged images of the quasicleavage fractured region, corresponding to the area enclosed by the squares in (a) and (b), respectively. The red dashed line indicates the location where the local plastic strain analysis was performed, as shown in Fig. 5.

FIGURE 6. Two-dimensional virtual cross sections of 3D strain maps of equivalent strain at each applied strain. (a)~(c) are cross-sections of 0.0 Mn analyzed at 2.2%, 5.6%, and 11.5% of applied strains, respectively. (d)~(f) are cross-sections of 0.6Mn analyzed at 2.2%, 7.7%, 10.7% of applied strains, respectively.

FIGURE 7. Vertical cross-sections of 3D mapping of (a) vacancy concentration, (b) geometrically necessary dislocations and (c) statistically stored dislocations at ε_a = 10.7%, where the strain quasicleavage crack initiated, in the 0.6Mn specimen.

FIGURE 8. Microstructure of the 0.0Mn alloy. (a) is a backscattered SEM image of Al_7Cu_2Fe and Mg_2Si particles dispersed in the matrix. (b) and (c) are HAADF-STEM images. A fully coherent η' phase and Al_3Zr were observed in (b), and a semicoherent η_2 phase was observed in (c).

FIGURE 9. Observed microstructures of the 0.6Mn specimen. (a) and (b) are backscattered electron images using SEM and HAADF–STEM, respectively. (c)~(i) are HAADF–STEM images and corresponding elemental maps of Mn-bearing particles ($Al_{20}Cu_2Mn_3$) using STEM–EDS.

FIGURE 10. Crystal models and calculated hydrogen trapping energies from DFT calculations. (a), (b), and (c) are the unit cells of $Al_{20}Cu_2Mn_3$, $Al_{12}Fe_3Si$, and $Al_{12}Mn_3Si$. A magnified image of the most strongly hydrogen-trapped site in each model is shown. (d) Calculated result of multiple hydrogen trapping at the strongest hydrogen trapping site for each model.

FIGURE 11. Hydrogen partitioning in 0.0Mn and 0.6Mn alloys just before fracture (ε_a = 11.5% for 0.0Mn and ε_a = 10.7% for 0.6Mn). (a) is the trapped hydrogen content and (b) is the hydrogen occupancy for each trap site. Note that the second-phase particle (IMC) of the 0.0Mn alloy was all Al_7Cu_2Fe, and the IMC of the 0.6Mn alloy was estimated as $Al_{12}(Fe, Mn)_3Si$, assuming that $Al_{12}Fe_3Si$ and $Al_{12}Fe_3Si$ are 50% each.

FIGURE 12. Relationship between the area fraction of quasicleavage fracture on the fracture surface and holding time.

10 TABLES

Table 1. Chemical composition of alloys used in this study (mass%).

	Si	Fe	Cu	Mn	Mg	Cr	Zn	Ti	Zr	Al
0.6Mn	0.06	0.04	1.52	0.63	2.44	<0.01	10.16	0.03	0.13	Bal.
0.0Mn	0.06	0.04	1.52	0.0	2.44	<0.01	10.16	0.03	0.13	Bal.

Table 2. Hydrogen trapping energy of each site in aluminum alloys.

Trap site	Trap energy, $E_{\mathrm{trap},\,i}$/eV·atom^{-1}	Ref.
Solute Mg	0.12	5
Edge dislocation	0.18	27
Screw dislocation	0.11	27
Vacancy	0.29	26
GB	0.23-0.27	29
Interior of $Al_{20}Cu_2Mn_3$	0.24	This work
Interior of $Al_{12}Fe_3Si_3$	0.36	This work
Interior of $Al_{12}Mn_3Si_3$	0.66	This work
Coherent interface of $MgZn_2$	0.08-0.35	5
Semicoherent interface of $MgZn_2$	0.55	6
Pore (aluminum surface)	0.70	30

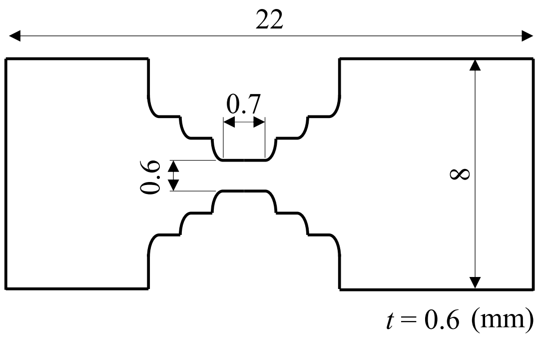

Fig. 1 Specimen geometry for the in situ tensile test in SPring-8.

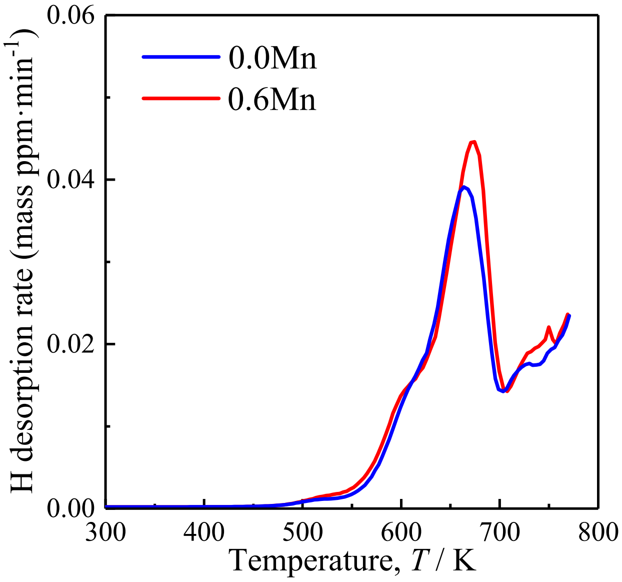

Fig. 2 TDA curves of prepared alloy with and without trace Mn to measure hydrogen content.

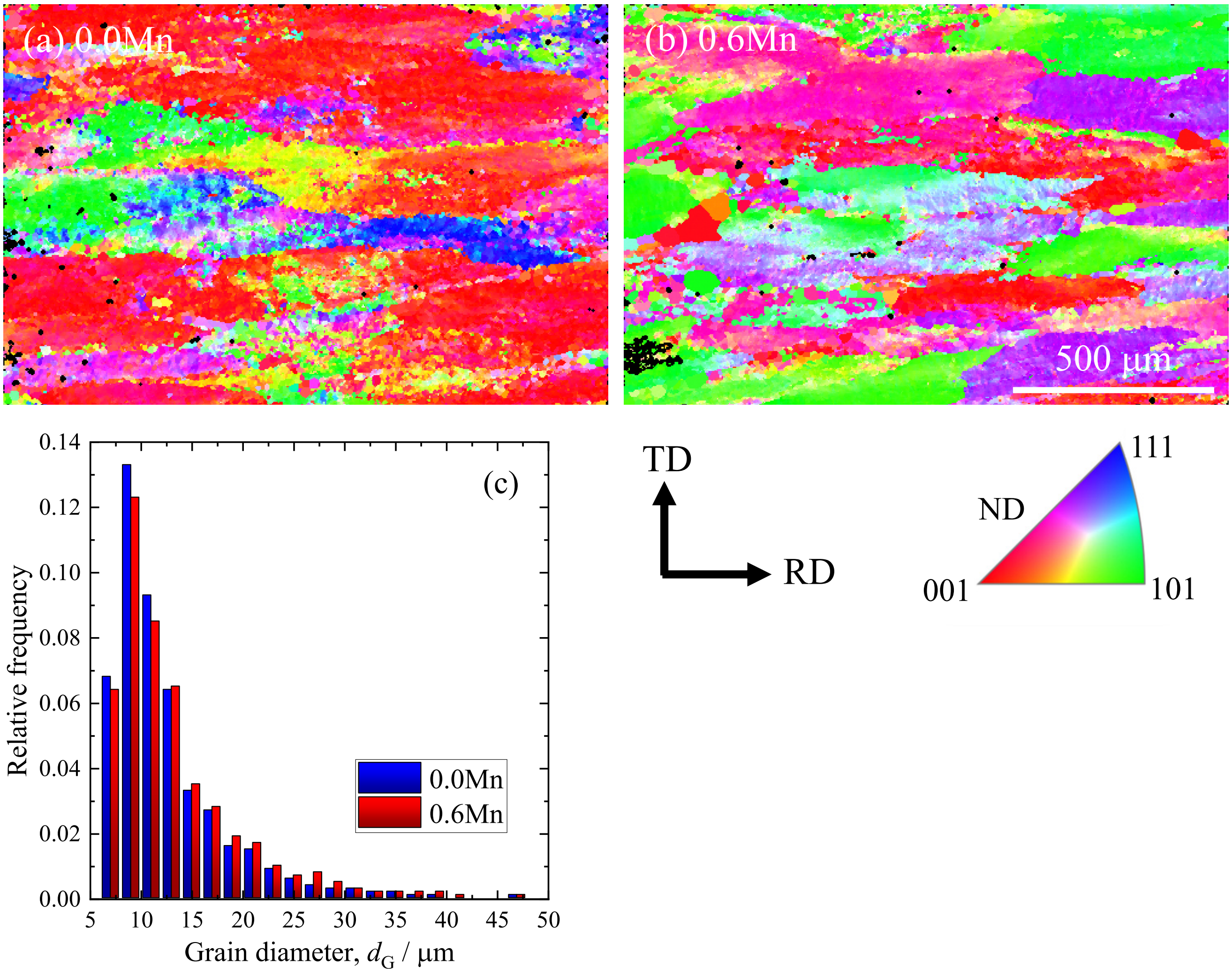

Fig. 3 EBSD analysis of 0.0Mn and 0.6Mn alloys. (a) and (b) are the inverse pole figure maps for the nominal direction (ND) of 0.0Mn and 0.6Mn alloys, respectively. (c) Grain-size distribution.

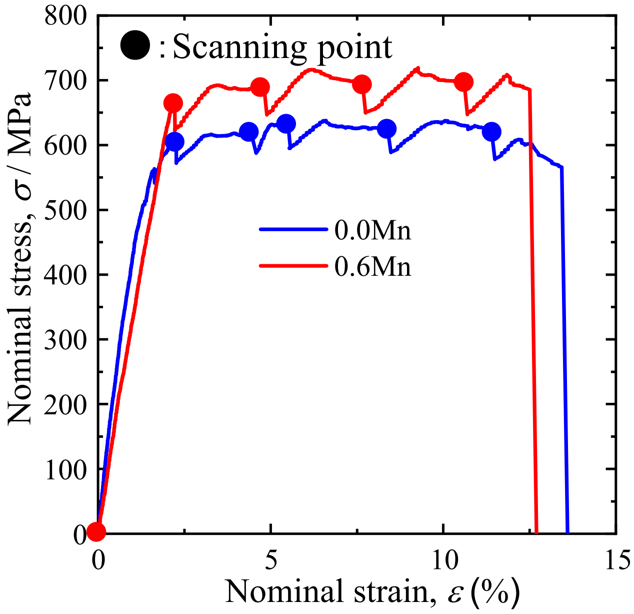

Fig. 4 Nominal stress-strain curves obtained from in-situ tensile tests using synchrotron X-ray CT. The closed dots indicate the strain stages at which the CT scan was performed, where the decrease in stress corresponds to stress relaxation during the scan.

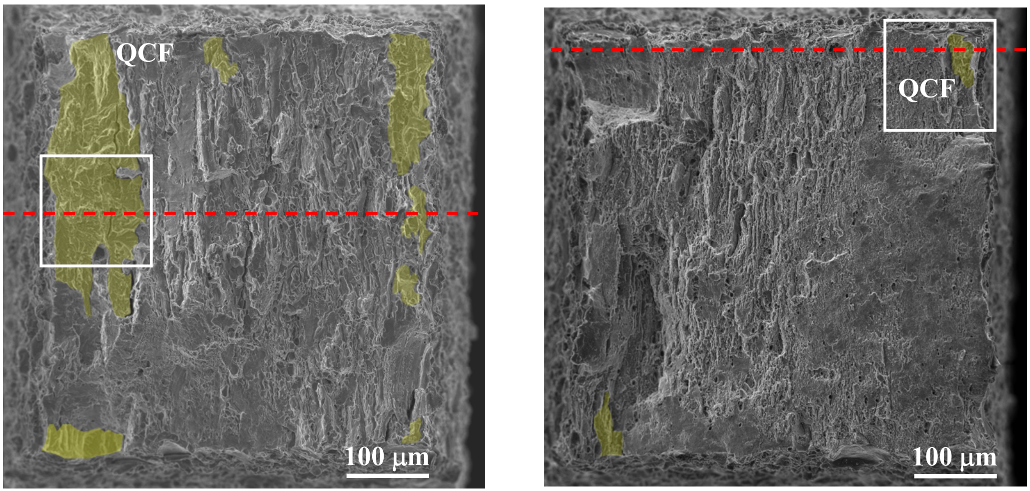

(a) 0.0Mn (b) 0.6Mn

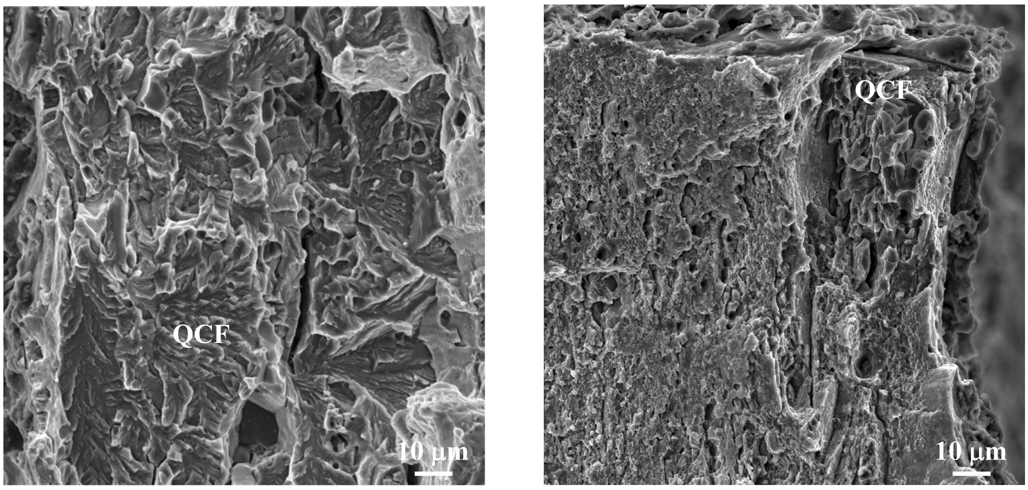

(c) Enlarged view of (a) (d) Enlarged view of (b)

Fig.5 SEM fractographs of the alloy of (a) 0.0Mn, (b) 0.6Mn. The yellow masked area is the region of quasicleavage fracture. (c) and (d) are enlarged images of the quasicleavage fractured region, corresponding to the area enclosed by the squares in (a) and (b), respectively. The red dashed line indicates the location where the local plastic strain analysis was performed, as shown in Fig. 5.

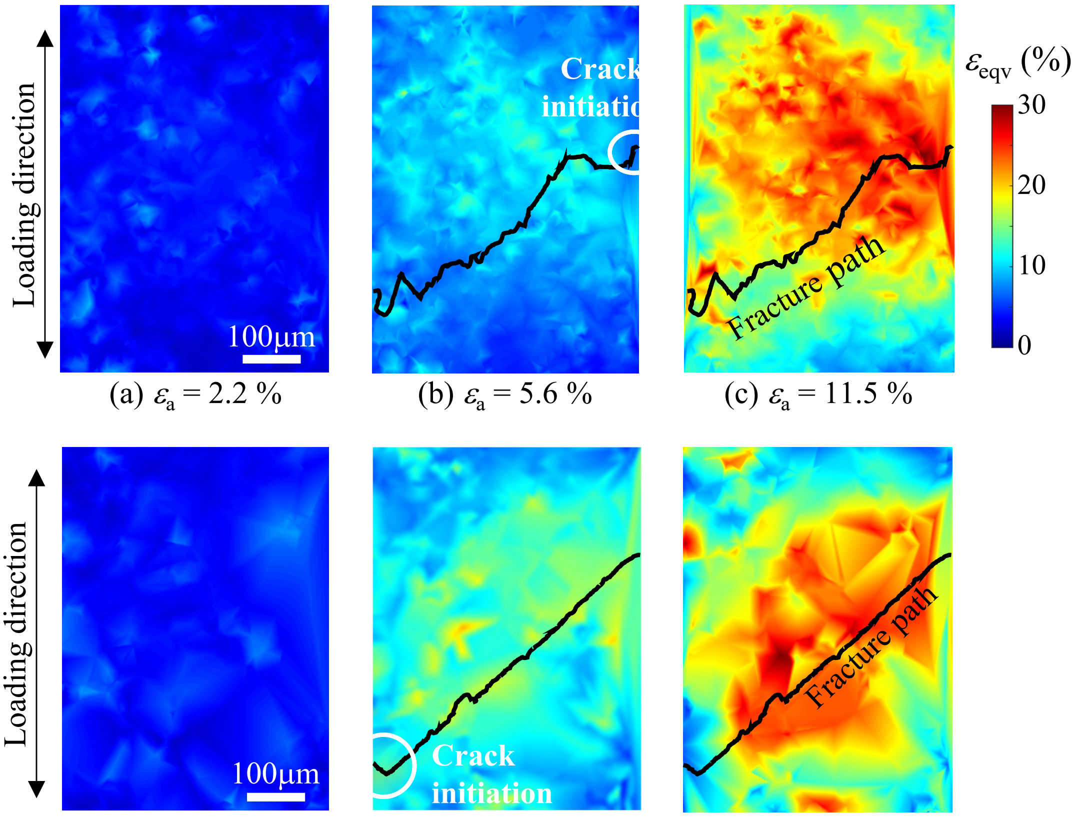

(a) $\varepsilon_a = 2.2$ % (b) $\varepsilon_a = 5.6$ % (c) $\varepsilon_a = 11.5$ %

(d) $\varepsilon_a = 2.2$ % (e) $\varepsilon_a = 7.7$ % (f) $\varepsilon_a = 10.7$ %

Fig. 6 Two-dimensional virtual cross sections of 3D strain maps of equivalent strain at each applied strain. (a)~(c) are cross-sections of 0.0Mn analyzed at 2.2%, 5.6%, 11.5% of applied strains, respectively. (d)~(f) are cross-sections of 0.6Mn analyzed at 2.2%, 7.7%, 10.7% of applied strains, respectively.

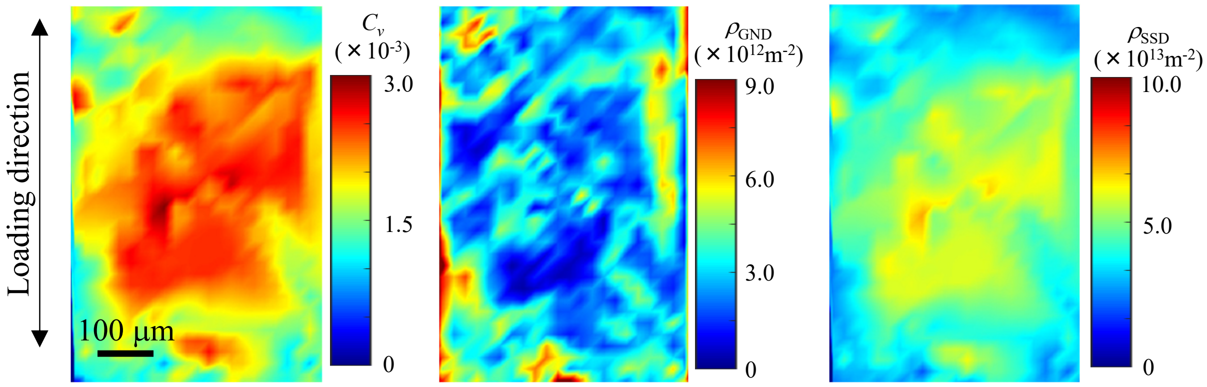

(a) Vacancy concentration (b) GND density (c) SSD density

Fig. 7 Vertical cross-sections of 3D mapping of (a) vacancy concentration, (b) geometrically necessary dislocations and (c) statistically stored dislocations at ε_{a} = 10.7%, where the strain quasicleavage crack initiated, in the 0.6Mn specimen.

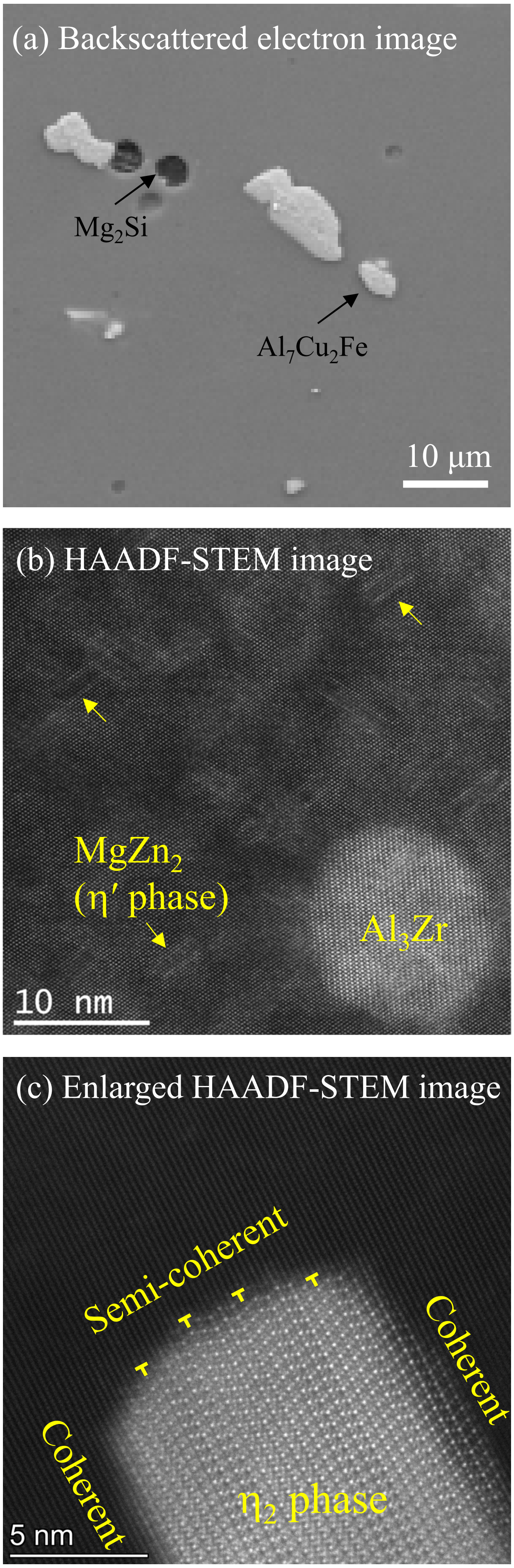

Fig. 8 Microstructure of the 0.0Mn alloy. (a) is backscattered SEM image of Al_7Cu_2Fe and Mg_2Si particles dispersed in the matrix. (b) and (c) are HAADF-STEM images. A fully coherent η′ phase and Al_3Zr were observed in (b) and semicoherent η_2 phase was observed in (c).

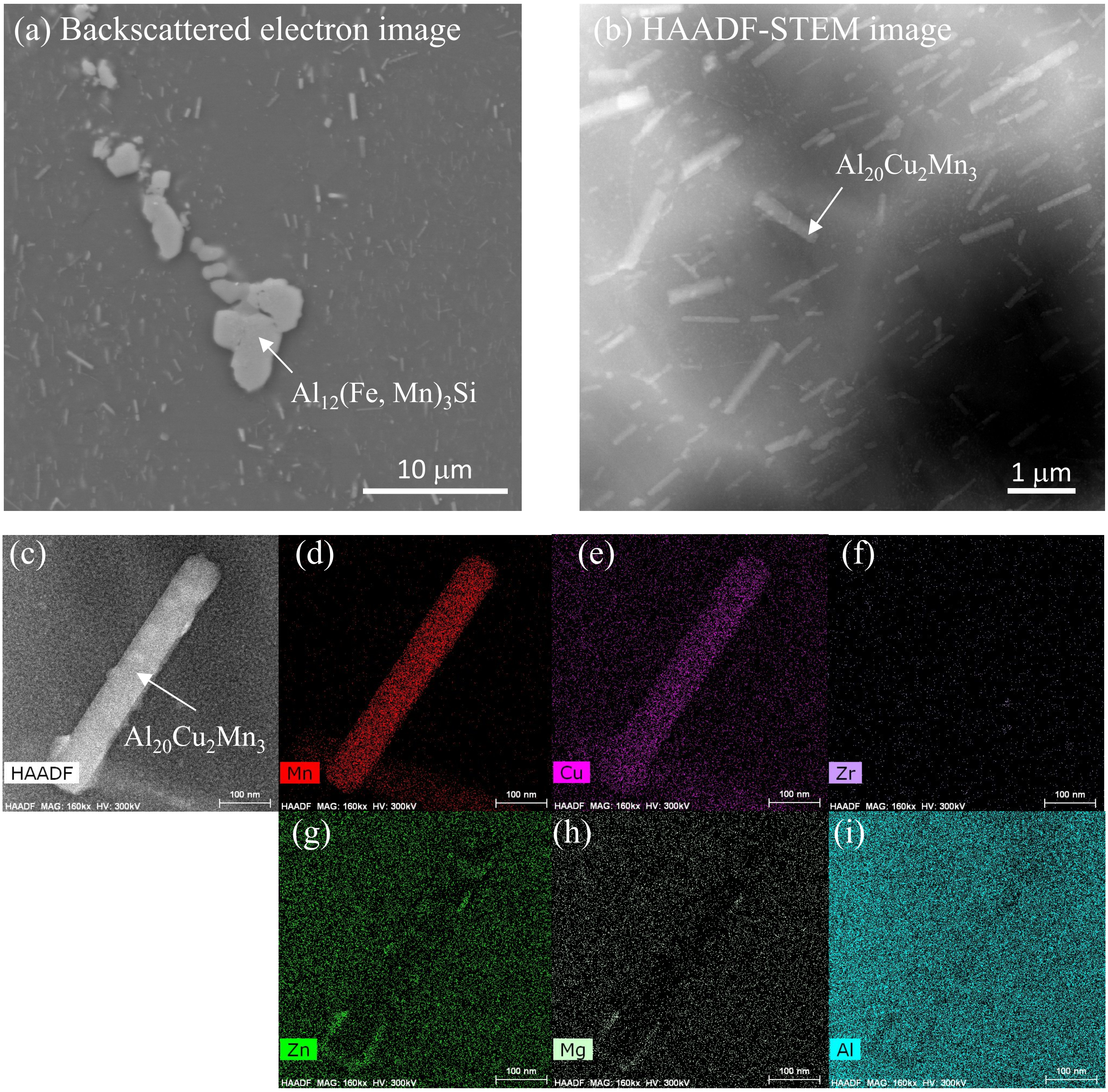

Fig. 9 Observed microstructures of the 0.6Mn specimen. (a) and (b) are backscattered electron image and HAADF-STEM images, respectively. (c)~(i) are HAADF-STEM image and corresponding elemental maps of Mn-bearing particles ($Al_{20}Cu_2Mn_3$) using STEM-EDS.

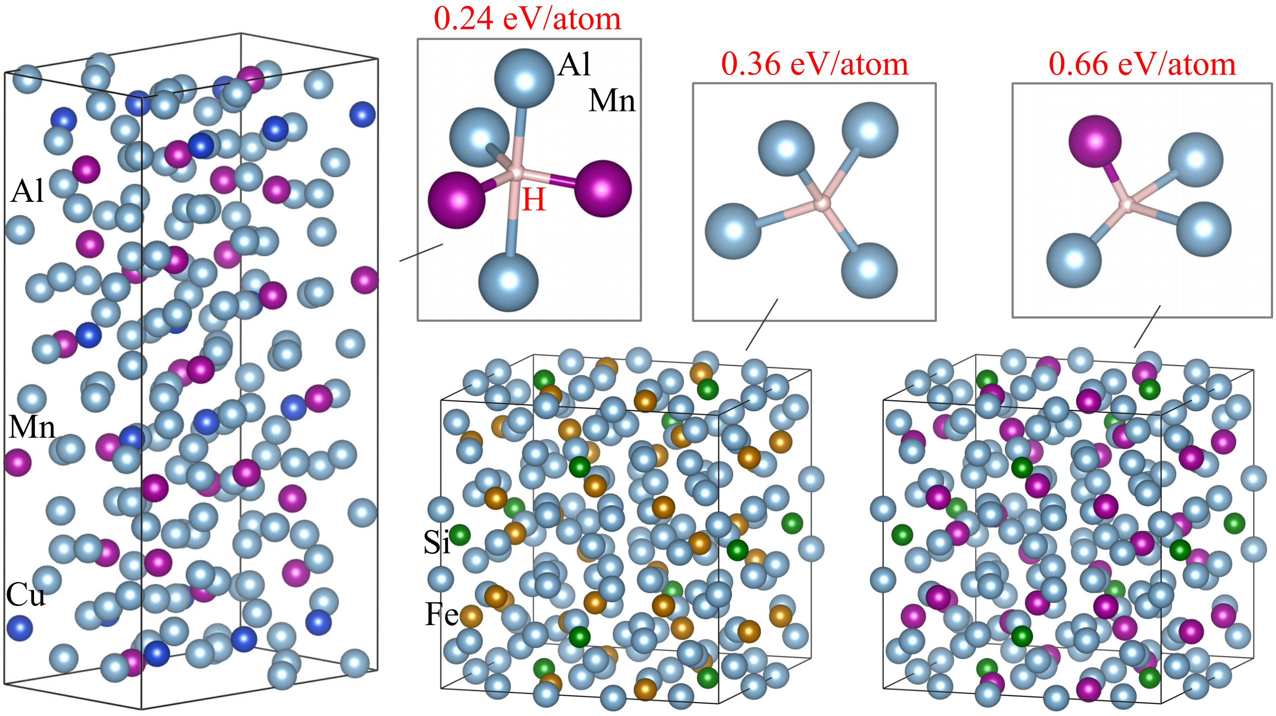

(a) $Al_{20}Cu_2Mn_3$ (b) $Al_{12}Fe_3Si$ (c) $Al_{12}Mn_3Si$

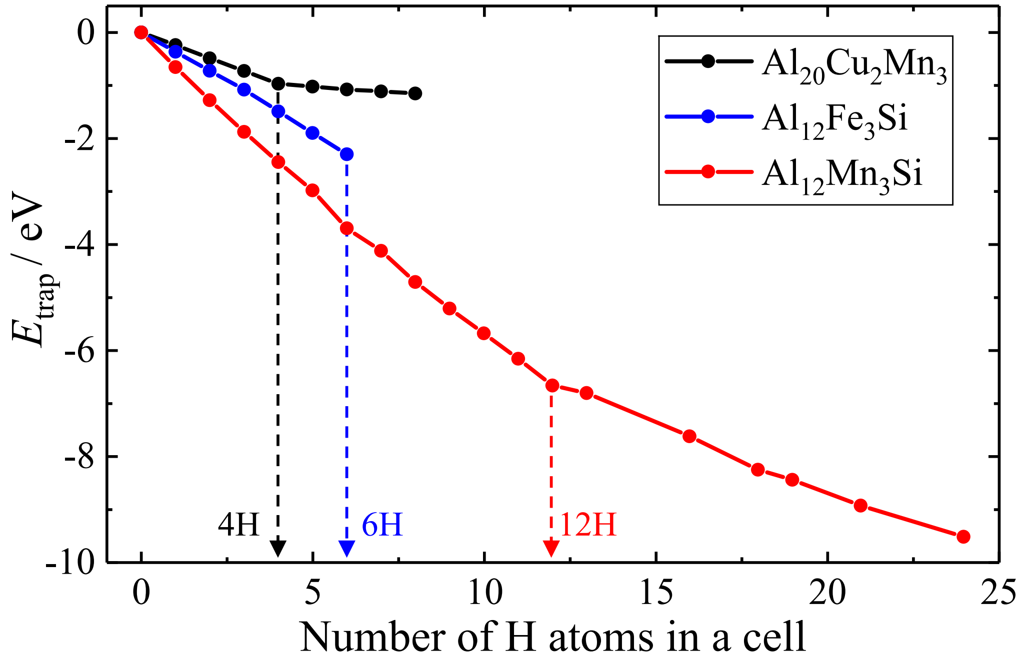

(d) multiple hydrogen trapping at each of the strongest hydrogen trapping sites

Fig. 10 Crystal models and calculated hydrogen trapping energies from DFT calculations. (a), (b), and (c) are the unit cells of $Al_{20}Cu_2Mn_3$, $Al_{12}Fe_3Si$, and $Al_{12}Mn_3Si$. A magnified image of the most strongly hydrogen-trapped site in each model is shown. (d) Calculated result of multiple hydrogen trapping at the strongest hydrogen trapping site for each model.

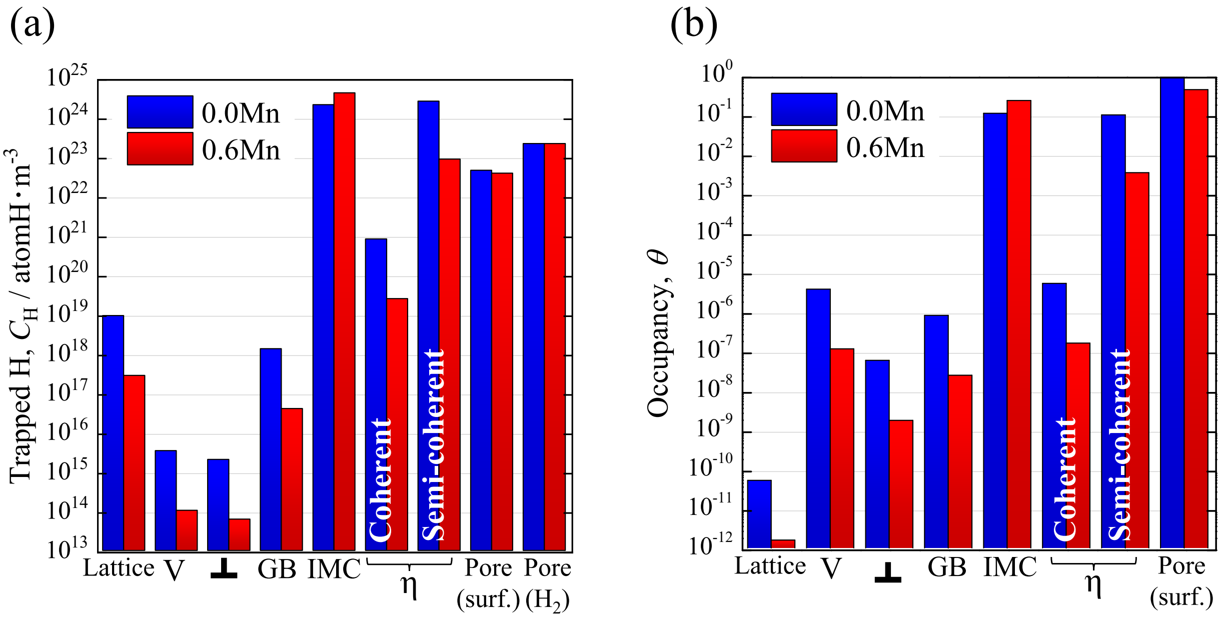

Fig.11 Hydrogen partitioning in 0.0Mn and 0.6Mn alloys just before fracture (ε_a = 11.5% for 0.0Mn and ε_a = 10.7% for 0.6Mn). (a) is the trapped hydrogen content and (b) is the hydrogen occupancy for each trap site. Note that the second phase particle (IMC) of the 0.0Mn alloy was all Al_7Cu_2Fe, and the IMC of the 0.6Mn alloy was estimated as $Al_{12}(Fe, Mn)_3Si$, assuming that $Al_{12}Fe_3Si$ and $Al_{12}Fe_3Si$ are 50% each.

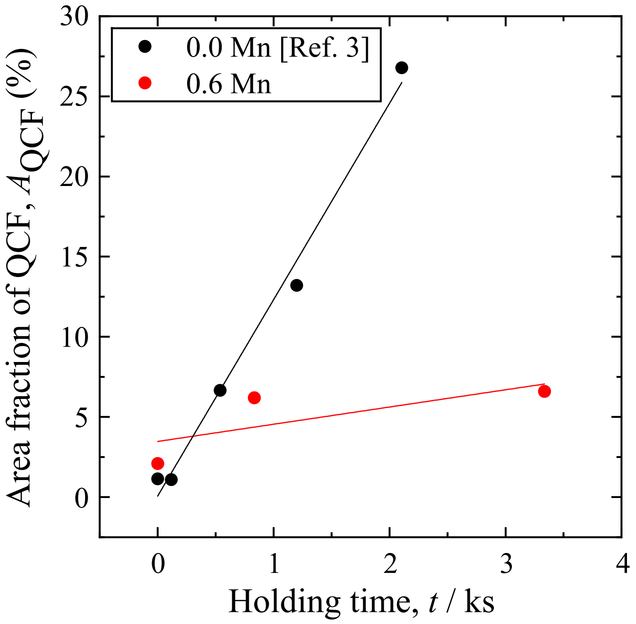

Fig.12 Relationship between the area fraction of quasicleavage fracture on the fracture surface and holding time.